Seismically-derived porosity of deep-sea sediments over the last 74 Ma in the equatorial Atlantic Ocean: Implications for paleo-climate

Giulia Matilde Ferrante, Satish C. Singh, Pranav Audhkhasi, Colin J. Thomson, Venkata Vaddineni, Milena Marjanović

▶ **To cite this version:**

Giulia Matilde Ferrante, Satish C. Singh, Pranav Audhkhasi, Colin J. Thomson, Venkata Vaddineni, et al.. Seismically-derived porosity of deep-sea sediments over the last 74 Ma in the equatorial Atlantic Ocean: Implications for paleo-climate. Earth and Planetary Science Letters, 2023, 612, 10.1016/j.epsl.2023.118163 . insu-04155707

HAL Id: insu-04155707

https://insu.hal.science/insu-04155707v1

Submitted on 31 Oct 2023

HAL is a multi-disciplinary open access archive for the deposit and dissemination of scientific research documents, whether they are published or not. The documents may come from teaching and research institutions in France or abroad, or from public or private research centers.

L'archive ouverte pluridisciplinaire **HAL**, est destinée au dépôt et à la diffusion de documents scientifiques de niveau recherche, publiés ou non, émanant des établissements d'enseignement et de recherche français ou étrangers, des laboratoires publics ou privés.

Supplementary Material for Seismically-derived porosity of deep-sea sediments over the last 74 Ma in the equatorial Atlantic Ocean: Implications for paleo-climate

Giulia Matilde Ferrante[a,b*], Satish C. Singh[a], Pranav Audhkhasi[a,c], Colin Thomson[d], Venkata Vaddineni[a], Milena Marjanović[a]

[a] *Université Paris Cité, Institut de Physique du Globe de Paris, 1 rue Jussieu, Paris, 75005, France*
[b] *Now at Istituto Nazionale di Oceanografia e Geofisica Sperimentale - OGS, 42c Borgo Grotta Gigante, 34010, Sgonico (TS), Italy*
[c] *Now at Shell Technology Centre, 7 Bengaluru Hardware Park KIADB Industrial Park North, Mahadeva Kodigahelli, Bengaluru, Karnataka, 562149, India*
[d] *41 Sherlock Close, Cambridge, CB3 0HP, U.K*

Contents

Supplementary Text S1-S5

Supplementary Figures S1-S10

Supplementary Tables S1-S2

References

Supplementary Text

S1. Seismic surveys and acquisition parameters

The data analysed in this work were collected during three seismic surveys: (1) the TransAtlantic ILAB deep-seismic survey (Profile 1, Mehouachi & Singh, 2018; Audhkhasi & Singh, 2019; Audhkhasi & Singh, 2022), (2) the LITHOS-ILAB refraction survey (Profile 1, Grevemeyer et al., 2019; Vaddineni et al., 2021), and (3) the ILAB-SPARC reflection-refraction survey (Profiles 2 and 3, Marjanović et al., 2020; Gregory et al., 2021; Growe et al., 2021; Wang et al., 2022; Wang & Singh, 2022).

During the TransAtlantic ILAB survey, 2750 km of ultra-deep seismic reflection data were acquired onboard WesternGeco M/V Western Trident in 2015, using a 12 km-long multi-sensor streamer with a receiver spacing of 3.125 m. The energy source consisted of six subarrays, each containing 8 air guns totalling to a volume of 10170 in^3, deployed at 15 m depth. The shot spacing varied from 50 to 75 m, depending on the age of the lithosphere. Most of the profile lies on the African Plate (0-75 Ma), crosses the ridge-axis, and samples the South American Plate (0-26 Ma). Portions of these MCS data have been used to study the crustal and

lithospheric structures along different part of the profile (Mehouachi & Singh, 2018; Audhkhasi & Singh, 2019; Marjanović et al., 2020; Audhkhasi & Singh, 2022).

The collocated OBS data were acquired aboard the German R/V Maria S. Merian during the LITHOS-ILAB experiment in 2017. A total of 71 OBSs were deployed along an 1100 km transect, with OBS spacing of 10-20 km. The data were sampled at 250 *Hz* for all the instruments. The seismic source consisted of six G-gun clusters (12 guns) configured as two sub-arrays with a total volume of 5440 in^3. The air-gun array was operated at 210 bar, towed at 7.5 m depth and fired every ~400 m along the profile.

The ILAB-SPARC survey was conducted in 2018 onboard the French N/O Pourquoi Pas? and both MCS and OBS data were acquired simultaneously along two perpendicular profiles. The MCS data were acquired using a 6 km-long streamer, towed at 12 m depth, with a receiver spacing of 6.25 m. The energy source consisted of two airgun sub-arrays, each with 9 airguns, with a total volume of 4990 in^3, towed at 15 m water depth and fired at 300 m interval. Although parts of these profiles were covered during TransAtlanticILAB ultra-deep seismic survey, we decided to use the ILAB-SPARC MCS data to have uniform and coincident coverage with the refraction data. The refraction survey consisted of 85 multi-component OBSs deployed at a spacing of 14-17 km.

S2. V_P-V_S ratio uncertainty

We calculated the uncertainty associated with $\frac{V_P}{V_S}$ by error propagation. It depends on the manual picking of the identified events in the OBS gathers and in the MCS stack sections. It can be written as follows:

$$d\left(\frac{V_P}{V_S}\right) = \sqrt{\left(\frac{\partial(V_P\,/\,V_S)}{\partial D}\,dD\right)^2 + \left(\frac{\partial(V_P\,/\,V_S)}{\partial(\,T_b - T_{sea}\,)}\,d(T_b - T_{sea})\right)^2}$$

$$= \sqrt{\left(\frac{2}{(\,T_b - T_{sea}\,)}\,dD\right)^2 + \left(\frac{-2D}{(\,T_b - T_{sea}\,)^2}\,d(T_b - T_{sea})\right)^2}$$

where $T_b - T_{sea}$ is the seafloor-to-basement two-way travel time (TWTT) beneath the OBS, D is the time delay between the P and P-to-S arrivals, *dD* is the uncertainty associated with the time delay D and $d(T_b - T_{sea})$ is the uncertainty associated with the seafloor-to-

basement TWTT sediment thickness $T_b - T_{sea}$.

For conventional travel-time tomography the picking errors on OBS gathers (*dD*) are normally 20-30 ms but here, because of the strong reverberatory nature of the P-to-S converted waves, we set it to 60 ms.

The uncertainty associated with picking sediment thickness from the MCS data $d(T_b - T_{sea})$ was calculated as following:

$$d(T_b - T_{sea}) = \sqrt{(2 * \text{MCS time sampling})^2 + (\text{OBS relocation uncertainty})^2}$$

where the MCS time sampling is equal to 8 ms and the OBS relocation uncertainty is the rms residual error of the least square fitting of water wave arrival picked in each OBS gather. We found that the uncertainty associated with $\frac{V_P}{V_S}$ is between 0.3 and 4.1.

S3. Porosity uncertainty

We calculated the uncertainty associated with porosity propagating the error through Eq. 3 of the main text (Lee, 2002). It depends on the $\frac{V_P}{V_S}$ uncertainties and it can be written as follows:

$$d(\phi) = \frac{C_1 C_2}{n} \left(\frac{V_P}{V_S}\right)^{-\left(1+\frac{1}{n}\right)} d\left(\frac{V_P}{V_S}\right)$$

where $C_1 = (3K + 4\mu)^{\frac{1}{2n}}$ and $C_2 = (3\mu G^2)^{-\frac{1}{2n}}$.

K and μ are the bulk and shear modulus of the matrix material and G and n are constants taking into account the degree of compaction and the effect of clay on velocities, respectively. Porosity values with relative uncertainty >10% (9 points in total, all of them at crustal ages < 17 Ma) are considered outliers and excluded from the analysis.

S4. Spearman correlation between porosity and climate proxies

We calculated the formal correlation coefficients of the porosity data with $\delta^{18}O$, $\delta^{13}C$ and CO_2 climate proxies in the age range 3-37 Ma. To do that, we used the Spearman's rank correlation coefficient, r_s, a nonparametric measure of rank correlation, which can assess both linear and non-linear monotonic relationship and it is weakly affected by outliers.

The results show positive correlation between the porosity and CO_2 (r_s = 0.665), a negative correlation between the porosity and $\delta^{13}C$ (r_s = -0.445), a weaker but still significant negative correlation between the porosity and $\delta^{18}O$ (r_s = -0.340).

S5. Limit of the method

For this work we have analysed a huge amount of MCS data (~2000 km) and 69 OBSs, covering oceanic crustal age from 3 to 74 Ma. To have consistent results over such a large spatial extent, we had to simplify the calculation. Furthermore, except for ODP sites 662 and 663, which cored down to the Late Pliocene, we do not have any direct measurements of the sediments. Therefore, our analysis required several approximations and assumptions.

First, the formula we used to calculate average $\frac{V_P}{V_S}$ in the sediments is valid only in a 1D-approximation and with the rays travelling vertically within the sedimentary sequence. However, layering in the sediment creates internal multiples and the long duration of the converted wave can be explained by the effects of wide-angle ringing in sediment wedges arising from dip on the basement-sediment interface. In other words, lateral variations matter and the location of an OBS relative to the underlying sediment pinch-outs or basin flattening can have a significant effect on the delay, strength and duration of the converted wave.

Secondly, we must underline that, in this work, we only considered average $\frac{V_P}{V_S}$ and average porosity in the sediments. Yet, over such a large spatial and temporal scale, the sedimentary column will encompass material characterised by a wide range of seismic velocities, density and porosity. We are aware that this is a severe limitation, but we do not have enough information to constrain the variation of such properties with depth. Instead, although we discussed the role of sediments input from Africa, which could be hemipelagic or turbiditic in origin, we made the basic and realistic assumption of dealing only with pelagic sediment. Redistribution of sediment (of the same lithology) via gravity-transport mechanisms, on the other hand, could be particularly important, especially where the seafloor topography is particularly rugged. The topographic highs may have some material removed by slumps and currents, and this material would accumulate in adjacent local basins. Our OBS spacing is not dense enough to appreciate this phenomenon. As the OBS stations were deployed at equal spacing, indistinctly located on topographic highs and lows, both $\frac{V_P}{V_S}$ and porosity are estimated on a regional scale. It would be an enormous task to characterise turbidites and slumps along our profiles, but their scientific impact would be limited.

In addition to the above approximations, we have assumed that in the sediments $\frac{V_P}{V_S}$ is a function of porosity only. In modelling the porosity, we also assumed the matrix bulk and shear moduli of clay material and we set the dimensional modelling parameters following the modelling studies for unconsolidated sediments with porosities greater than 40% (Lee, 2002). However, we performed a parametric study on these 4 parameters (matrix bulk and shear moduli, n, G), finding that the sensibility of Eq. 3 to these is quite low.

Supplementary Figures

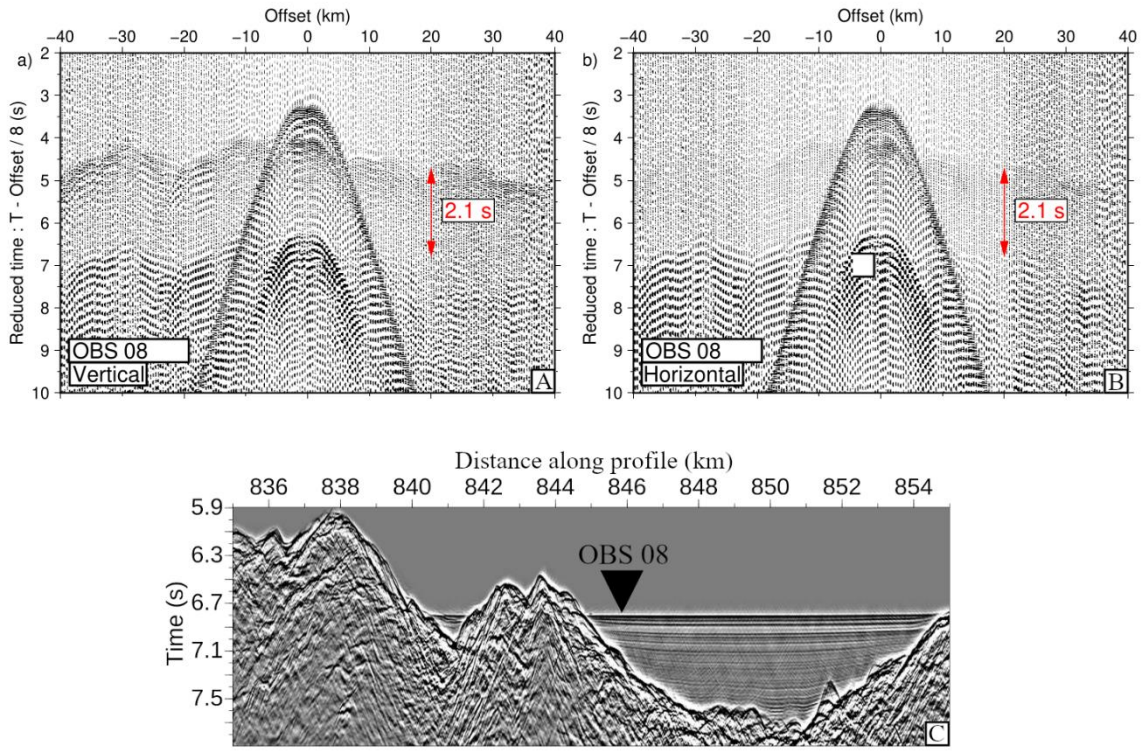

Figure S1: A) Vertical component of seismic data at OBS 08, B) horizontal component. The distance is from the OBS location. The sediment delay is marked. C) MCS image showing the location of OBS 08 along Profile 1.

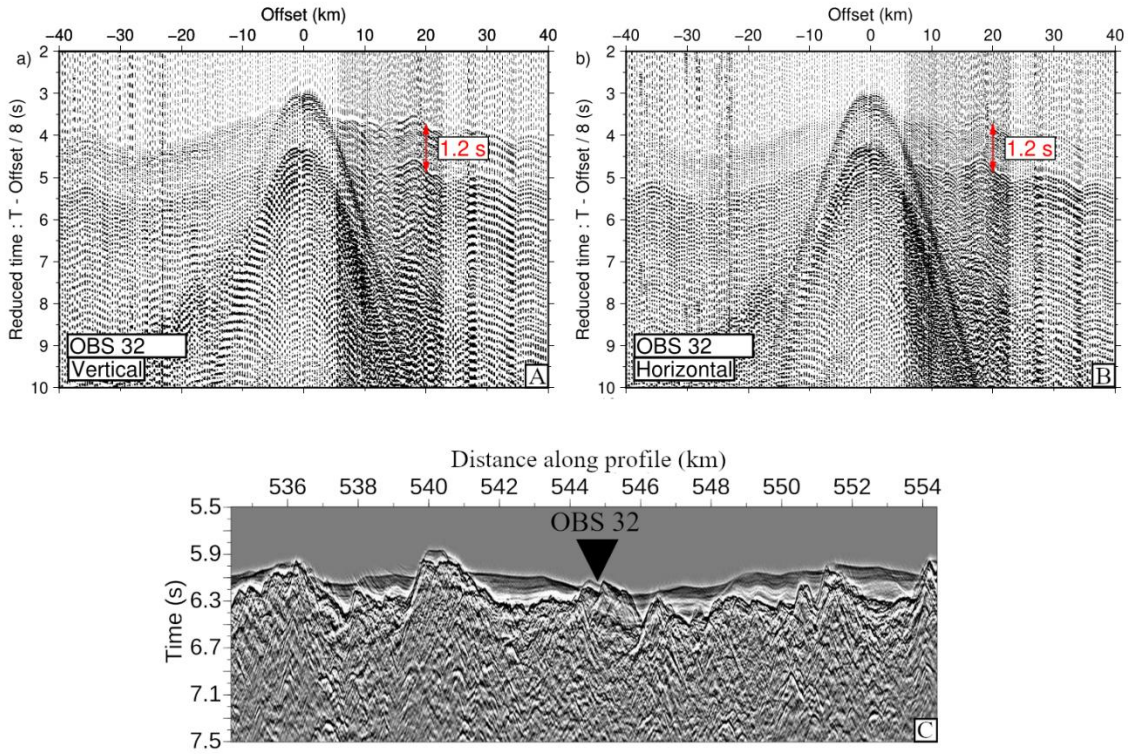

Figure S2: A) Vertical component of seismic data at OBS 32, B) horizontal component. The distance is from the OBS location. The sediment delay is marked. C) MCS image showing the location of OBS 32 along Profile 1.

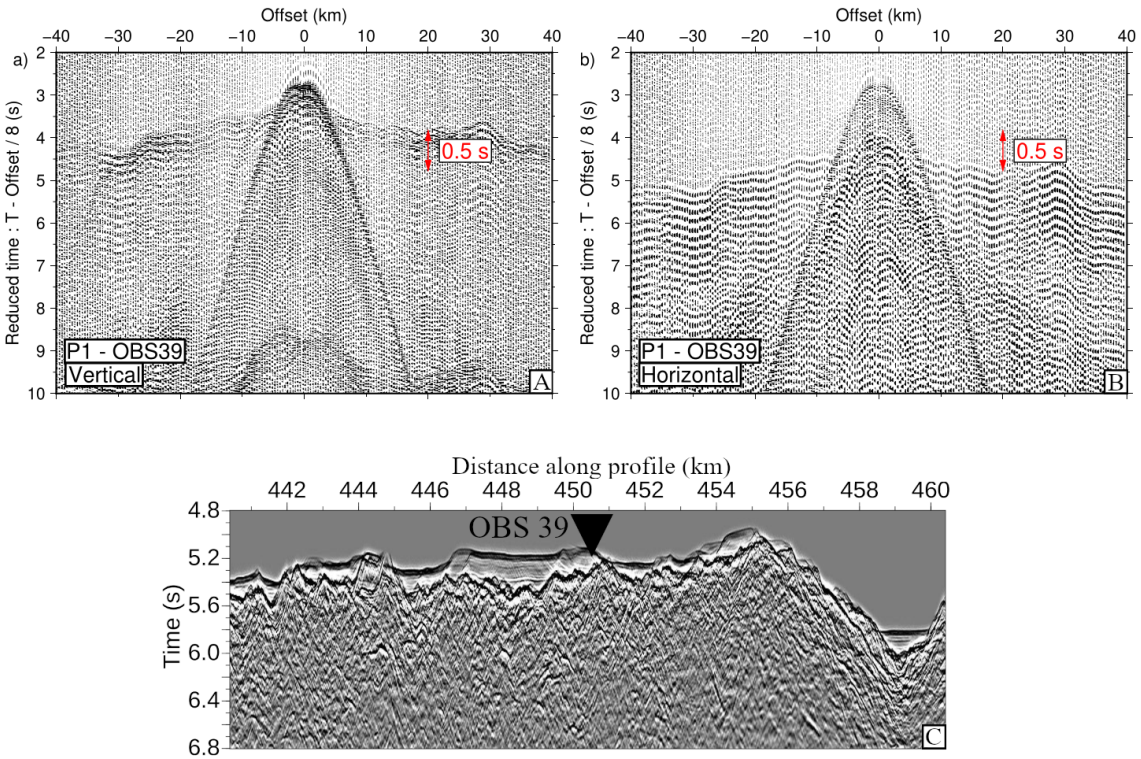

Figure S3: A) Vertical component of seismic data at OBS 39, B) horizontal component. The distance is from the OBS location. The sediment delay is marked. C) MCS image showing the location of OBS 39 along Profile 1.

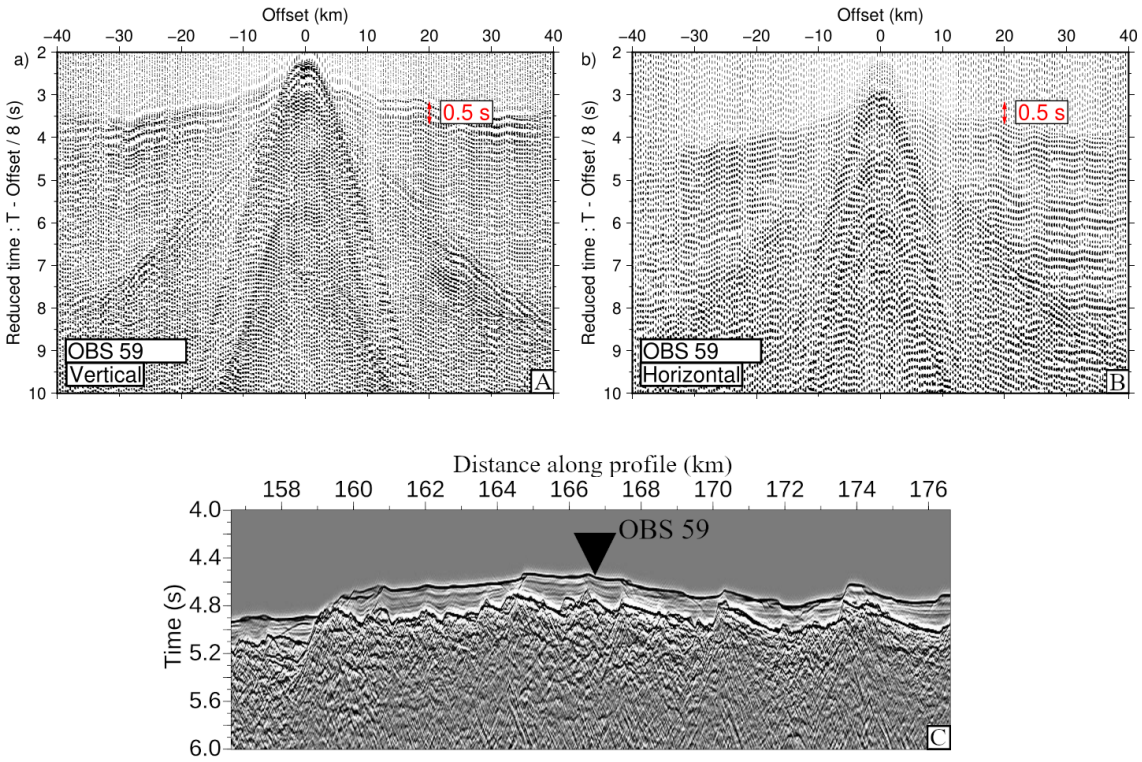

Figure S4: A) Vertical component of seismic data at OBS 59, B) horizontal component. The distance is from the OBS location. The sediment delay is marked. C) MCS image showing the location of OBS 59 along Profile 1.

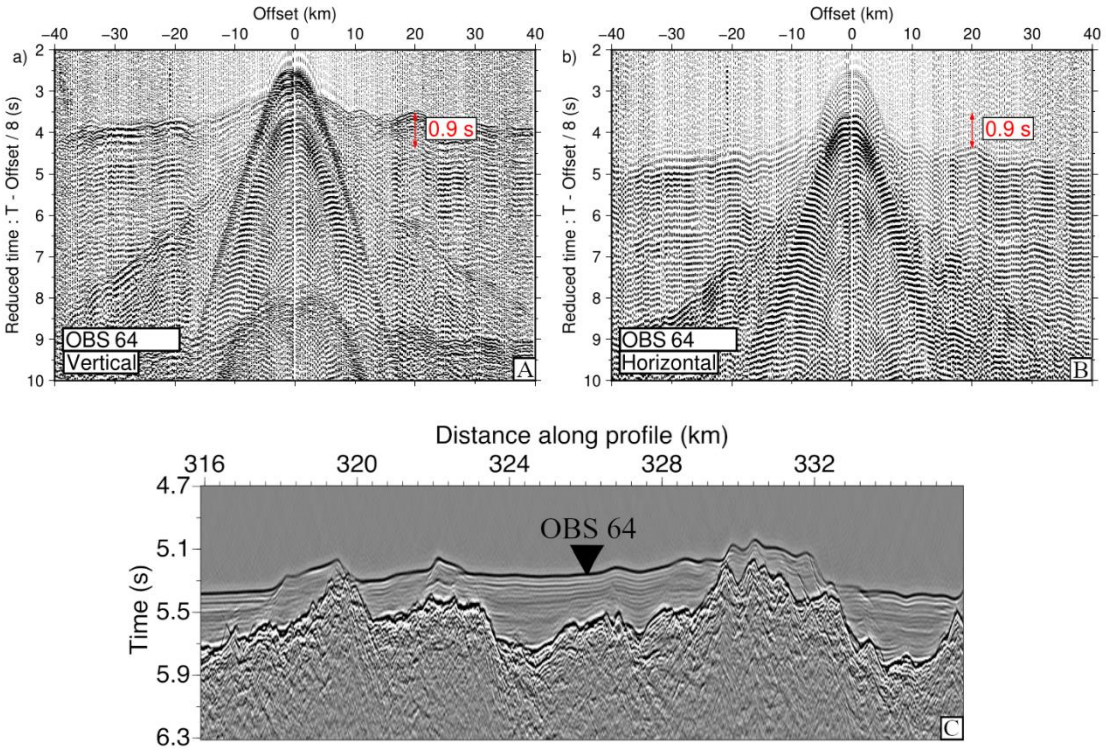

Figure S5: A) Vertical component of seismic data at OBS 64, B) horizontal component. The distance is from the OBS location. The sediment delay is marked. C) MCS image showing the location of OBS 64 along Profile 2.

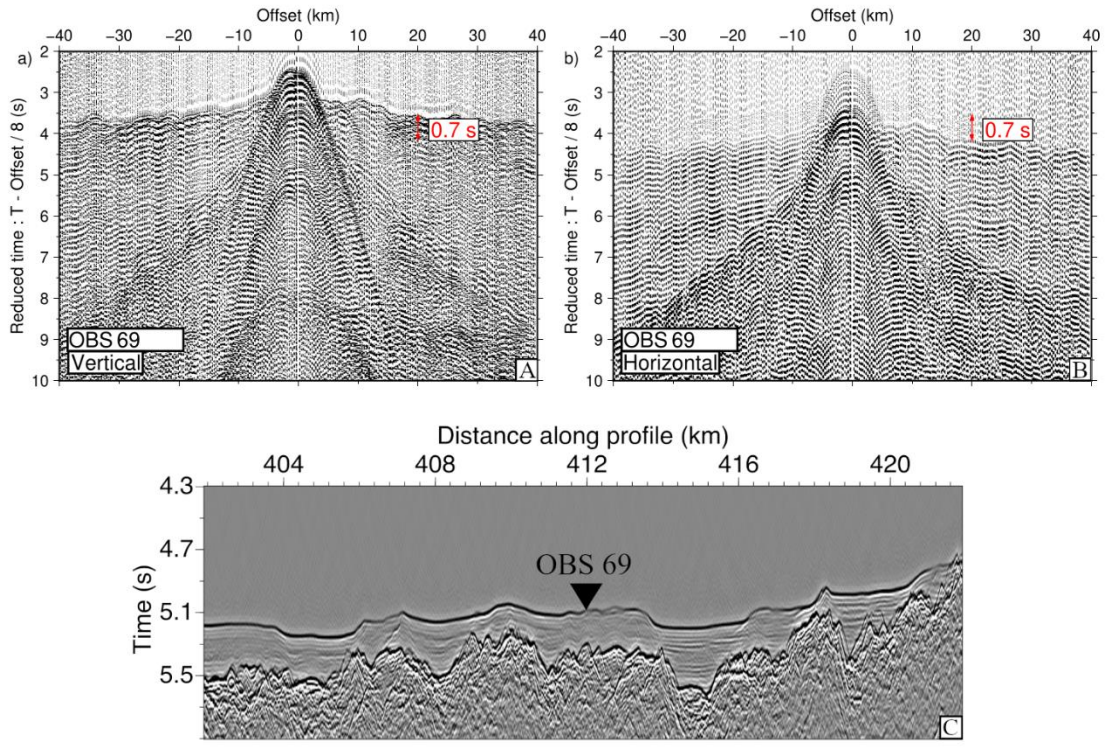

Figure S6: A) Vertical component of seismic data at OBS 69, B) horizontal component. The distance is from the OBS location. The sediment delay is marked. C) MCS image showing the location of OBS 69 along Profile 2.

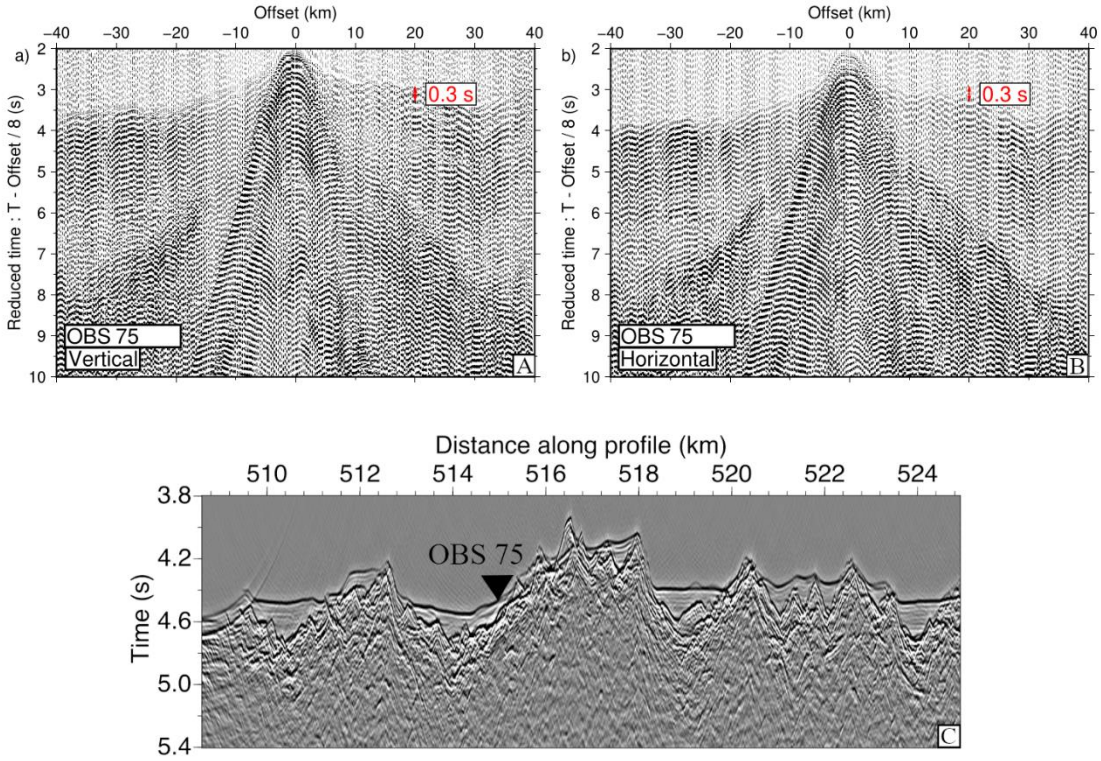

Figure S7: A) Vertical component of seismic data at OBS 75, B) horizontal component. The distance is from the OBS location. The sediment delay is marked. C) MCS image showing the location of OBS 75 along Profile 2.

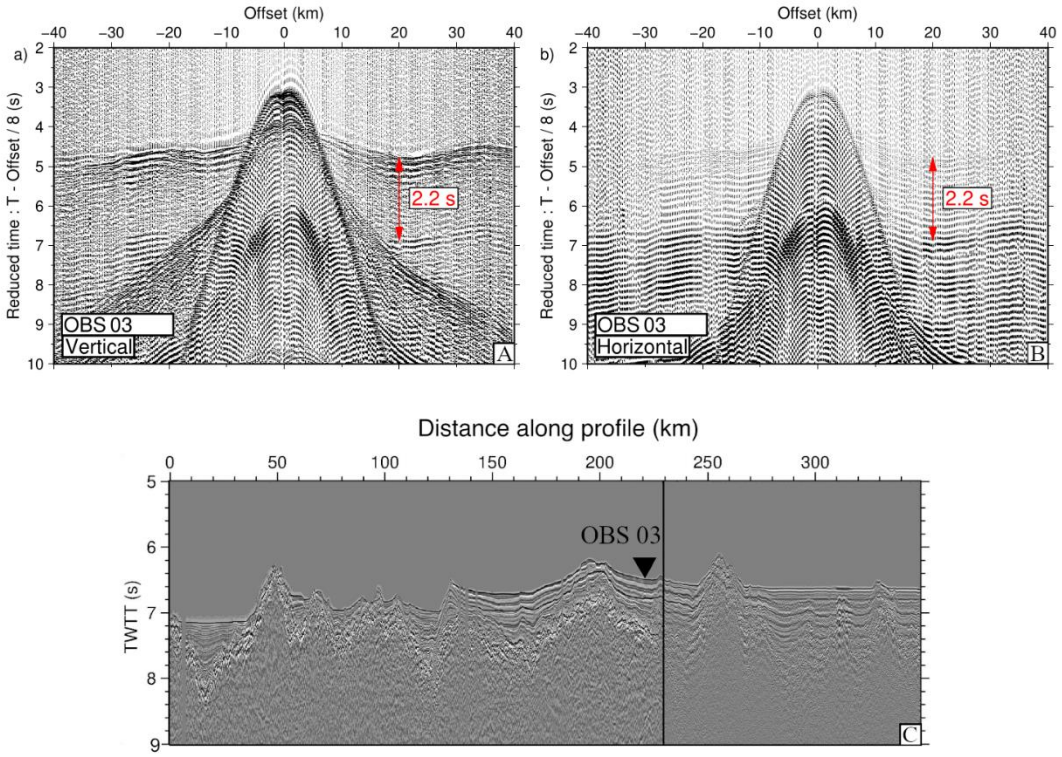

Figure S8: A) Vertical component of seismic data at OBS 03, B) horizontal component. The distance is from the OBS location. The sediment delay is marked. C) MCS image showing the location of OBS 03 along Profile 3 (modified from Growe et al., 2021).

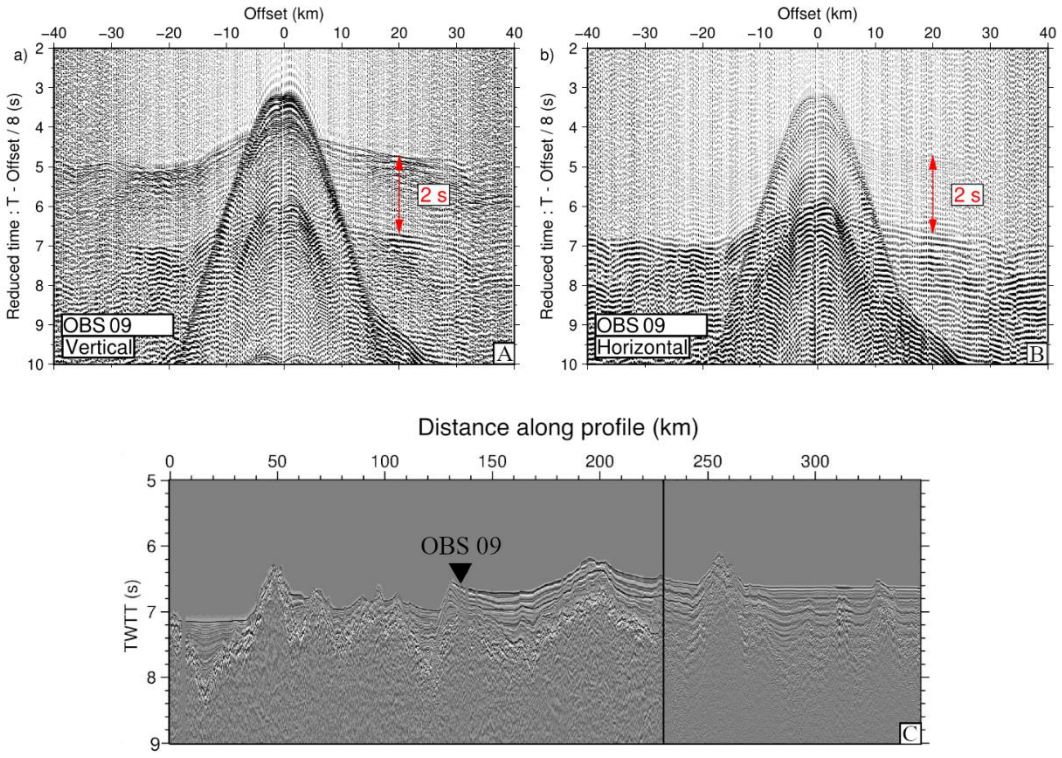

Figure S9: A) Vertical component of seismic data at OBS 09, B) horizontal component. The distance is from the OBS location. The sediment delay is marked. C) MCS image showing the location of OBS 09 along Profile 3 (modified from Growe et al., 2021).

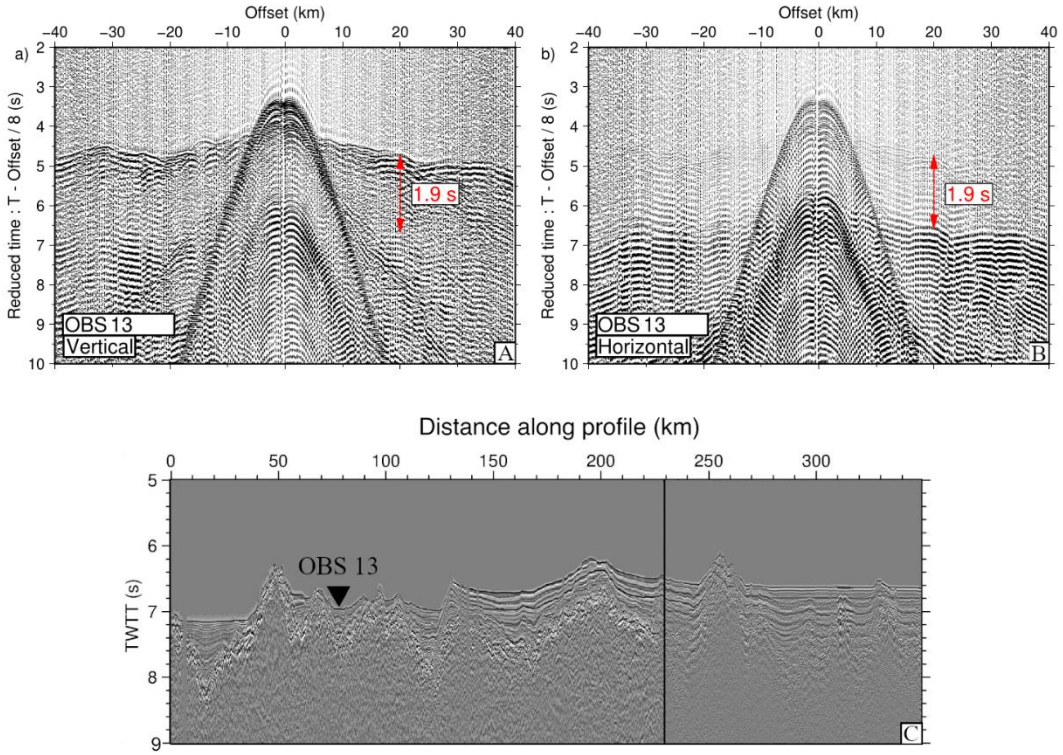

Figure S10: A) Vertical component of seismic data at OBS 13, B) horizontal component. The distance is from the OBS location. The sediment delay is marked. C) MCS image showing the location of OBS 13 along Profile 3 (modified from Growe et al., 2021).

Supplementary Tables

S1: Data

Age (Ma)	MCS TWT (s)	OBS delay (s)	$\frac{V_P}{V_S}$	$\frac{V_P}{V_S}$ uncert.	ϕ	ϕ uncert.	OBS n°	Profile n°	Deploy LON	Deploy LAT	Reloc. LON	Reloc. LAT	Reloc. uncert. (s)
3.0	0.16	0.63	8.88	1.99	0.763	0.053	76	2	-13.4509	-1.4212	-13.4515	-1.4209	0.03392
4.0	0.15	0.48	7.40	1.92	0.716	0.074	83	2	-12.3960	-1.1742	-12.3963	-1.1744	0.03772
4.5	0.13	0.29	5.46	1.36	0.615	0.096	75	2	-13.6016	-1.4564	-13.6031	-1.4564	0.02433
5.0	0.21	0.61	6.81	1.47	0.691	0.067	84	2	-12.2453	-1.1389	-12.2464	-1.1398	0.04640
5.5	0.12	0.52	9.67	2.08	0.782	0.047	74	2	-13.7523	-1.4917	-13.7546	-1.4912	0.01950
6.5	0.30	0.67	5.47	0.78	0.615	0.055	73	2	-13.9030	-1.5269	-13.9059	-1.5263	0.04189
7.5	0.18	0.54	7.00	1.66	0.699	0.071	72	2	-14.0538	-1.5621	-14.0563	-1.5617	0.04277
7.5	0.13	0.67	11.31	1.57	0.814	0.026	60	1	-11.0144	-2.4670	-11.0137	-2.4661	0.00148
8.5	0.18	0.52	6.78	0.85	0.690	0.039	59	1	-10.9266	-2.4474	-10.9257	-2.4467	0.00243

8.5	0.26	0.72	6.54	0.88	0.678	0.043	71	2	-14.2045	-1.5973	-14.2074	-1.5976	0.03112
9.0	0.30	0.52	4.47	0.44	0.529	0.046	58	1	-10.8387	-2.4278	-10.8378	-2.4269	0.00127
10.0	0.16	0.59	8.38	1.07	0.749	0.032	57	1	-10.7509	-2.4082	-10.7499	-2.4073	0.00459
10.5	0.23	0.71	7.17	0.88	0.707	0.036	69	2	-14.5060	-1.6677	-14.5083	-1.6669	0.02075
10.5	0.24	0.80	7.67	0.67	0.726	0.024	56	1	-10.6630	-2.3886	-10.6621	-2.3878	0.00133
11.0	0.27	0.44	4.26	0.48	0.506	0.056	55	1	-10.5752	-2.3690	-10.5746	-2.3684	0.00157
11.5	0.29	0.72	5.97	0.90	0.647	0.053	68	2	-14.6567	-1.7028	-14.6582	-1.7025	0.04398
11.5	0.22	0.37	4.36	0.60	0.518	0.066	54	1	-10.4874	-2.3493	-10.4867	-2.3486	0.00212
13.5	0.23	0.74	7.43	0.69	0.717	0.026	52	1	-10.1800	-2.2806	-10.1719	-2.2733	0.00223
13.5	0.14	0.25	4.57	1.46	0.540	0.147	66	2	-14.9582	-1.7732	-14.9593	-1.7721	0.04339
14.5	0.13	0.66	11.15	3.92	0.811	0.066	65	2	-15.1090	-1.8083	-15.1087	-1.8104	0.04606
15.0	0.21	0.67	7.38	0.75	0.715	0.029	50	1	-9.9165	-2.2216	-9.9171	-2.2222	0.00224
15.0	0.35	0.90	6.14	0.55	0.657	0.030	64	2	-15.2598	-1.8434	-15.2606	-1.8421	0.02413
15.5	0.15	0.44	6.87	1.72	0.694	0.077	49	1	-9.7848	-2.1921	-9.7844	-2.1917	0.03536
17.0	0.26	0.52	5.00	1.00	0.579	0.084	47	1	-9.5213	-2.1330	-9.5203	-2.1343	0.05511
17.0	0.31	0.58	4.74	0.51	0.556	0.048	62	2	-15.5614	-1.9136	-15.5623	-1.9129	0.02259
19.0	0.10	0.59	12.80	2.30	0.836	0.029	44	1	-9.1262	-2.0443	-9.1251	-2.0431	0.00445
20.0	0.11	0.67	13.18	2.14	0.840	0.026	43	1	-8.9945	-2.0147	-8.9934	-2.0135	0.00451
20.5	0.10	0.52	11.40	2.08	0.815	0.034	42	1	-8.8628	-1.9851	-8.8617	-1.9840	0.00332
20.5	0.31	1.43	10.23	1.38	0.794	0.028	58	2	-16.1646	-2.0538	-16.1664	-2.0547	0.04170
21.0	0.24	1.11	10.25	0.82	0.795	0.017	41	1	-8.7311	-1.9555	-8.7295	-1.9539	0.00578
21.0	0.21	0.99	10.43	1.54	0.798	0.030	40	3	-17.2652	-1.8797	-17.2689	-1.8789	0.02753
22.0	0.20	0.56	6.60	1.08	0.681	0.052	56	2	-16.4662	-2.1239	-16.4678	-2.1251	0.02755
22.0	0.23	0.74	7.43	0.71	0.717	0.027	40	1	-8.5994	-1.9259	-8.5982	-1.9245	0.00658
22.5	0.24	1.11	10.25	0.85	0.795	0.017	39	1	-8.4678	-1.8963	-8.4670	-1.8971	0.00759
23.0	0.13	0.42	7.46	1.64	0.718	0.062	55	2	-16.6170	-2.1589	-16.6177	-2.1595	0.02217
23.5	0.19	0.96	11.11	1.47	0.810	0.025	38	1	-8.3361	-1.8667	-8.3366	-1.8652	0.01913
24.0	0.21	0.52	5.95	0.72	0.646	0.043	37	1	-8.2044	-1.8370	-8.2034	-1.8303	0.00894
24.0	0.37	1.07	6.78	0.66	0.690	0.030	54	2	-16.7679	-2.1938	-16.7672	-2.1948	0.03348
24.5	0.15	0.93	13.40	2.39	0.843	0.028	53	2	-16.9187	-2.2288	-16.9178	-2.2288	0.02213
25.5	0.09	0.43	10.56	4.06	0.801	0.077	52	2	-17.0696	-2.2638	-17.0679	-2.2645	0.03241
26.0	0.12	0.56	10.33	2.31	0.796	0.045	43	3	-17.2097	-2.2320	-17.2112	-2.2313	0.02143
26.5	0.27	1.48	11.96	1.03	0.824	0.015	33	1	-7.6778	-1.7184	-7.6701	-1.7164	0.01618
26.9	0.16	1.07	14.38	2.08	0.854	0.021	49	3	-17.0899	-2.9931	-17.0880	-2.9909	0.01676
27.5	0.22	1.21	12.00	1.34	0.825	0.020	32	1	-7.5461	-1.6887	-7.5448	-1.6884	0.01851
29.5	0.16	1.19	15.88	2.26	0.867	0.019	29	1	-7.1512	-1.5996	-7.1503	-1.5988	0.01636
30.5	0.17	1.48	18.41	2.05	0.886	0.013	27	1	-6.8879	-1.5401	-6.8879	-1.5397	0.00990
32.5	0.20	1.26	13.60	1.59	0.845	0.018	24	1	-6.4931	-1.4509	-6.4940	-1.4511	0.01699
33.5	0.20	1.26	13.60	2.19	0.845	0.025	23	1	-6.3615	-1.4211	-6.3632	-1.4219	0.02941
34.0	0.30	2.15	15.33	4.09	0.863	0.037	22	1	-6.2298	-1.3913	-6.2306	-1.3915	0.08378
36.5	0.16	1.11	14.88	2.40	0.859	0.023	18	1	-5.7912	-1.2920	-5.7894	-1.2915	0.02081
37.5	0.20	1.85	19.50	2.78	0.892	0.015	15	1	-5.5280	-1.2324	-5.5275	-1.2320	0.02462
38.0	0.37	1.85	11.00	0.93	0.809	0.016	14	1	-5.4402	-1.2126	-5.4396	-1.2117	0.02816
38.5	0.21	1.70	17.19	196.31	0.878	1.398	13	1	-5.3525	-1.1927	-5.3349	-1.1748	2.54620
39.5	0.33	1.63	10.88	0.95	0.807	0.017	11	1	-5.1771	-1.1529	-5.1783	-1.1526	0.02458
40.0	0.55	2.59	10.42	0.60	0.798	0.012	10	1	-5.0016	-1.1131	-5.0033	-1.1136	0.02875
40.5	0.11	0.76	14.82	3.64	0.858	0.035	20	3	-17.6681	0.6858	-17.6706	0.6861	0.02256

41.0	0.35	2.07	12.83	0.93	0.836	0.012	16	3	-17.7478	1.1932	-17.7495	1.1927	0.01992
42.0	0.75	2.14	6.71	0.33	0.686	0.015	8	1	-4.6508	-1.0336	-4.6541	-1.0334	0.03400
46.0	0.40	1.85	10.25	1.64	0.795	0.033	4	1	-3.9490	-0.8743	-3.9479	-0.8740	0.06804
47.0	0.62	1.85	6.97	1.17	0.698	0.051	3	1	-3.7736	-0.8344	-3.7736	-0.7946	0.11910
48.0	0.30	1.40	10.33	0.93	0.796	0.018	14	3	-17.7877	1.4470	-17.7899	1.4465	0.02152
48.5	0.35	1.85	11.57	0.95	0.818	0.015	13	3	-17.8076	1.5738	-17.8066	1.5738	0.02452
54.5	0.67	2.14	7.39	0.35	0.715	0.013	10	3	-17.8675	1.9544	-17.8703	1.9547	0.02738
65.0	0.49	1.95	8.96	0.43	0.765	0.011	9	3	-17.8874	2.0813	-17.8773	2.0839	0.01497
70.5	0.66	2.57	8.79	0.34	0.760	0.009	7	3	-17.9273	2.3350	-17.9379	2.3350	0.01833
71.0	0.58	1.75	7.03	0.33	0.701	0.014	5	3	-17.9672	2.5887	-17.9711	2.5910	0.01808
72.0	0.52	1.68	7.46	0.38	0.718	0.014	4	3	-17.9872	2.7155	-17.9865	2.7179	0.01796
73.0	0.68	2.21	7.50	0.30	0.719	0.011	3	3	-18.0072	2.8424	-18.0129	2.8441	0.02045
74.0	0.75	2.25	7.00	0.29	0.699	0.012	2	3	-18.0271	2.9693	-18.0213	2.9726	0.02490

S2: Average porosity values divided per time range.

Time range (Ma)	Average porosity	Average porosity with outliers
3-17	0.69	0.65
19-21	0.81	/
22-24	0.71	/
24.5-36.5	0.83	/
37.5-74	0.78	/

References

Audhkhasi, P., Singh, S.C., 2019. Seismic structure of the upper crust from 0-75 Ma in the Equatorial Atlantic Ocean on the African Plate using ultra long offset seismic data. Geochemistry, Geophysics, Geosystems 20. doi:10.1029/2019GC008577.

Audhkhasi, P., Singh, S.C., 2022. Discovery of distinct lithosphere-asthenosphere boundary and the Gutenberg discontinuity in the Atlantic Ocean. Science Advances. 8. doi:10.1126/sciadv.abn5404.

Gregory, E.P.M., Singh, S.C., Marjanović, M., Wang, Z., 2021. Serpentinized peridotite versus thick mafic crust at the Romanche oceanic transform fault. Geology 49 (9). doi:10.1130/G49097.1.

Grevemeyer, I., Singh, S.C., Papenberg, C. (2019). Ocean bottom seismometer and ocean bottom hydrophone seismic refraction and wide-angle data from profile P02 of Maria S. Merian cruise MSM69 with links to sgy data files. PANGAEA. doi:10.1594/PANGAEA.907944.

Growe, K., Grevemeyer, I., Singh, S.C., Marjanović, M., Gregory, E.P.M., Papenberg, C., et al., 2021. Seismic structure of the St. Paul fracture zone and late Cretaceous to mid Eocene oceanic crust in the equatorial Atlantic Ocean near 18°W. Journal of Geophysical Research: Solid Earth 126. doi:10.1029/2021JB022456.

Lee, M.W. Modified Biot-Gassmann Theory for Calculating Elastic Velocities for Unconsolidated and Consolidated Sediments. Marine Geophysical Researches 23, 403–412 (2002). doi:10.1023/B:MARI.0000018195.75858.12

Marjanović, M., Singh, S.C., Gregory, E.P.M., Grevemeyer, I., Growe, K., Wang, Z., Vaddineni, V., Laurencin, M., Carton, H., Gómez de la Peña, L., Filbrandt, C., 2020. Seismic Crustal Structure and Morphotectonic Features Associated With the Chain Fracture Zone and Their Role in the Evolution of the Equatorial Atlantic Region. Journal of Geophysical Research: Solid Earth 125(10). doi:10.1029/2020JB020275.

Mehouachi, F., and Singh, S.C., 2018. Water-rich sublithospheric melt channel in the equatorial Atlantic Ocean. Nature Geoscience 11. doi:10.1038/s41561-017-0034-z.

Vaddineni, V.A., Singh, S.C., Grevemeyer, I., Audhkhasi, P., Papenberg, C., 2021. Evolution of the crustal and upper mantle seismic structure from 0–27 Ma in the equatorial Atlantic Ocean at 2° 43′S. Journal of Geophysical Research: Solid Earth 126. doi:10.1029/2020JB021390.

Wang, Z., Singh, S.C., Prigent, C. et al., 2022. Deep hydration and lithospheric thinning at oceanic transform plate boundaries. Nature Geoscience. 15. doi:10.1038/s41561-022-01003-3.

Wang, Z., and Singh, S.C., 2022. Seismic evidence for uniform crustal accretion along slow-spreading ridges in the equatorial Atlantic Ocean. Nature Communications 13, 7809. doi:10.1038/s41467-022-35459-z.